

# Sandwiched Graphene Clad Laminate: A Binder-Free Flexible Printed Circuit Board for 5G Antenna Application

Rongguo Song, Xin Zhao, Zhe Wang, Huaqiang Fu, Kunkun Han, Wei Qian, Suyan Wang, Jie Shen,\* Boyang Mao, and Daping He\*

Metal substitution is always the focus of scientific research in printed circuit board (PCB) and 5G communication technology. It is proved that the high thermal conductive carbon-based materials can be potential alternatives. However, the relatively low electrical conductivity and the difficulties in integrating carbon-based materials to functional substrates limit their further and industrial applications. Herein, a method is developed to fabricate large-scale, binder-free, flexible graphene clad laminate (GCL) by hot pressing assistant under vacuum to achieve excellent electrical properties and well-connected interface for PCB application, thus accomplishing metal substitution. GCL is a sandwich structure construct of top and bottom layers of high-conductivity graphene assembled film as a conductive layer and a dielectric substrate layer. A 5G millimeter wave antenna array based on GCL PCB operated at 26 GHz is designed, fabricated, and characterized. The GCL antenna array has a reflection coefficient of  $-20.98$  dB and a realized gain of  $11.05$  dBi, which are comparable to the metal antenna array made of the commercial copper clad laminate-based PCB. All the measurement results show that the flexible and lightweight GCL can be used as a new generation PCB for flexible electronic devices and radio frequency devices.

metal waste is becoming a severe problem, as it can cause significant environment pollutions.<sup>[4–6]</sup> Metal materials also suffer from high prices (because of their limited reserves), relatively poor flexibility, large density, and easily oxidized. As communication technologies developing, copper and other traditional metals-based PCB are becoming difficult to meet the new requirements for 5G communication devices, such as of being lightweight, flexible, miniaturized, and chemically stable under certain severe conditions.<sup>[7]</sup> Therefore, it is necessary to find a suitable material to realize metal substitution in the field of electronic products based on PCB.

Many attempts have been made to find the right candidates for such substitution of copper so far. Recently, carbon-based allotropic materials, such as carbon nanotubes (CNTs), carbon fibers, graphene, and fullerenes, have been widely investigated in the fields of antennas,<sup>[8–10]</sup> sensors,<sup>[11,12]</sup> transistors,<sup>[13]</sup> and other electronic fields,<sup>[14,15]</sup> given that they are abundant in nature and their advanced properties of lightweight, corrosion resistant, and environmental friendly. For instance, CNTs not only have excellent mechanical properties, biocompatibility, and chemical stability,<sup>[16–18]</sup> but also have the disadvantages of low conductivity, complex film-forming process, and high contact resistance.<sup>[19–21]</sup> Fullerenes, such as the CNTs, also suffer from low conductivity and difficult film forming,<sup>[22]</sup> which lead to the problems of high loss and unsatisfactory performance

## 1. Introduction

Printed circuit board (PCB), as the basic mechanically supports of electronic devices, is widely used in circuit, radio frequency (RF), and other fields.<sup>[1,2]</sup> Copper is the most commonly used conductive material in the PCB structure due to its high electrical conductivity and matured manufacture techniques.<sup>[3]</sup> Despite the advantages, with the increasing demand of electronic products,


lead to the problems of high loss and unsatisfactory performance

Dr. R. Song  
School of Information Engineering  
Hubei Engineering Research Center of RF-Microwave Technology and Application  
Wuhan University of Technology  
Wuhan 430070, China

Dr. X. Zhao, Dr. Z. Wang, H. Fu, W. Qian, Prof. D. He  
Hubei Engineering Research Center of RF-Microwave Technology and Application  
Wuhan University of Technology  
Wuhan 430070, China  
E-mail: hedaping@whut.edu.cn

K. Han, S. Wang, Prof. J. Shen  
State Key Laboratory of Advanced Technology for Materials Synthesis and Processing  
Wuhan University of Technology  
Wuhan 430070, China  
E-mail: shenjje@whut.edu.cn

Dr. B. Mao  
Department of Engineering  
University of Cambridge  
Cambridge CB3 0FA, UK

 The ORCID identification number(s) for the author(s) of this article can be found under <https://doi.org/10.1002/adem.202000451>.

DOI: 10.1002/adem.202000451

of the device. As graphene can offer the characteristics of low density, highest thermal conductivity, good structural flexibility, and high mechanical and chemical stabilities,<sup>[23–25]</sup> it has become the most promising material as a substitution for metals in electronic filed. Comparing with other carbon-based materials, one benefit of graphene is that it can be facily fabricated into film format in meter scale. Most recently, Lin and co-workers used a quasi-industrial film casting method to manufacture graphene assembled film (GAF) in a large area with a length of more than 2 m.<sup>[26]</sup> In addition, many methods have been proposed to fabricate graphene film in an efficient way.<sup>[27–29]</sup> In our previous works, we developed the freestanding GAFs with high conductive.<sup>[7,30]</sup> It is worth noting that this film-like format is important, as it is the standard pattern used in PCB fabrication at electronic industry.

In addition to conductivity and film format, another major problem for further application of graphene film in PCB is how to transfer the meter-scale freestanding graphene film onto a substrate with minimized electrical properties lose. Current methods for this procedure are to glue conductive layers and substrate with tape, which largely affects the system's dielectric constant stability.<sup>[8]</sup> In addition, such method is challenging to achieve large-scale production, thus hindering the developments of graphene-based PCB. Another way is to print graphene ink directly on the substrate, where the conductivity is very low and, thus, has poor performance.<sup>[31]</sup> Here, we propose a metal-free and binder-free graphene clad laminate (GCL) based on high conductivity GAF as conductive layers for PCB application. The clad laminate structure was fabricated by hot pressing under vacuum to achieve the assembly of GAF and substrate. Compared with the vacuum hot rolling,<sup>[32]</sup> vacuum hot pressing can accurately control the temperature and pressure. Such structure can

be directly applied as PCB and fabricated in meter scale with required pattern according to further application. By applying this GCL-based PCB, we proposed a 5G millimeter wave antenna array and demonstrated through experimental analysis that the GCL antenna array operates at 26 GHz, which adapts the millimeter waveband of 5G wireless communication. The reflection coefficient, bandwidth, radiation patterns, and gain of the proposed antenna array were also measured and showed comparable properties to their copper counterparts based on copper clad laminate (CCL)-based PCB. Flexible and lightweight graphene PCB and 5G antenna proposed in this work will be of great significance for PCB industry, wireless communication, flexible electronics, and wearable devices.

## 2. Results and Discussion

In our proposed GCL structure, GAFs function as the conductive layer, which requires high conductivity and excellent flexibility. **Figure 1a** shows the transmission electron microscope (TEM) image of graphene oxide (GO) sheet with the size of 30  $\mu\text{m}$ , which serves as the precursor. The left column of **Figure 1b** is the digital photograph of flexible GAF with the state of stamped, showing that the film is freestanding without substrate. Moreover, the GAF can be folded into a flower shape, as shown on the top-right panel of **Figure 1b**. After being stamped and clustered, the GAF was not damaged, and the surface remained intact as presented in the bottom-right panel of **Figure 1b**, indicating that the prepared GAF exhibits high flexibility and mechanical stability. During the process of high temperature annealing, due to the interconnection of the graphene sheets,

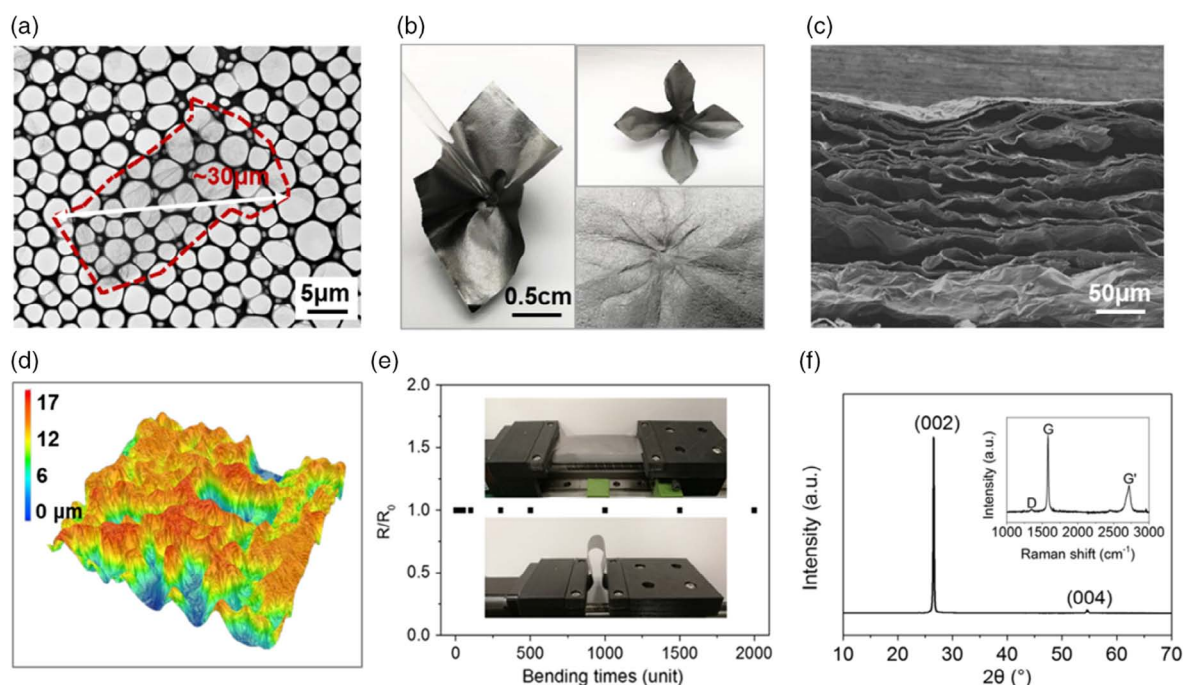


**Figure 1.** a) TEM image of GO sheet with a transverse dimension of 30  $\mu\text{m}$ . b) Digital photograph of GAF with the state of stamping and clustering. c) Cross-sectional SEM image of GAF with abundant micro-gasbags. d) Superlarge depth image of GAF shows undulating rough surface. e) Flexibility and stability test of GAF. f) XRD pattern and Raman spectra (inset) of GAF.

the synergistic effect of the gradual healing of the defects and the gas overflow causes the graphene film to generate extensive micro-gasbags, as shown in Figure 1c. Figure 1d and Figure S1, Supporting Information, show the superlarge depth image and surface scanning electron microscopy (SEM) image of GAF, which indicate that the GAF has undulating rough surface. To further verify the mechanical stability, a bending test of GAF is carried out. As shown in Figure 1e, after 2000 times bending with a bending radius of 10 mm at a frequency of 1 Hz, the resistivity remains almost constant, indicating that the GAF performs excellent flexibility. We also measure the electrical conductivity of the GAF via using a four-probe method; the measured values are  $1.76 \times 10^5 \text{ S m}^{-1}$ . To get the structural information, X-ray diffraction (XRD) and Raman spectra results are obtained. As shown in Figure 1f, the sharp and strong diffraction peak at  $26.5^\circ$  in XRD pattern indicates that the  $d_{002}$  of GAF is 0.336 nm, and the peak of (004) proves the highly graphitized structure of GAF. In the inset of Figure 1f, the Raman spectrum shows a strong diffraction G peak at  $1585 \text{ cm}^{-1}$  and a very low D peak at  $1335 \text{ cm}^{-1}$ , which demonstrates that the prepared GAF has very few lattice defects and is with a highly  $sp^2$  hybridized carbon atoms structure.

The GCL is fabricated by hot pressing, as shown in Figure 2a. First, the GAF with undulating rough surface (Figure S1) as the top and bottom layers are placed on both sides of the dielectric substrate with no additional binder. The sample

is then pressed under a series of pressures and temperatures stages and cools to room temperature gradually to obtain the GCL structure. The rough surface of GAF facilitates the binding and enhances the connection at the interface with the substrate, thus achieving a good adhering. Comparing with the traditional chemical etching method, the antenna and other devices based on GCL are manufactured by one-step laser engraving, described in Methods, which is fast, environmental friendly, and cost efficiency, as shown in Figure 2a and Figure S2, Supporting Information. As can be seen from the cross-sectional SEM image shown in Figure 2b, after hot pressing, sandwiched GCL is constructed by two layers of GAF conductive layers with the thickness of  $\approx 25 \mu\text{m}$  and an intermediate dielectric substrate layer. The conductive layers and dielectric layer compounded well with no binder and air gap, as shown in Figure 2c,d, which ensures a stable and controllable dielectric constant for further preparation of RF devices and circuits. The stable bonding between GAF layers and substrate layer also improves the flexibility and stability of GCL. The inset of Figure 2e and Figure S3, Supporting Information, are the digital photographs of GCL in the dimensions of  $16 \text{ cm} \times 10 \text{ cm}$ , presenting high flexibility. In addition, Figure 2f shows the GCL being carved into various devices while still maintaining such high flexibility. It is proved that GCL used as PCB can be the potential applied in the field of flexible electronic devices. Furthermore, top-view SEM images of GCL are

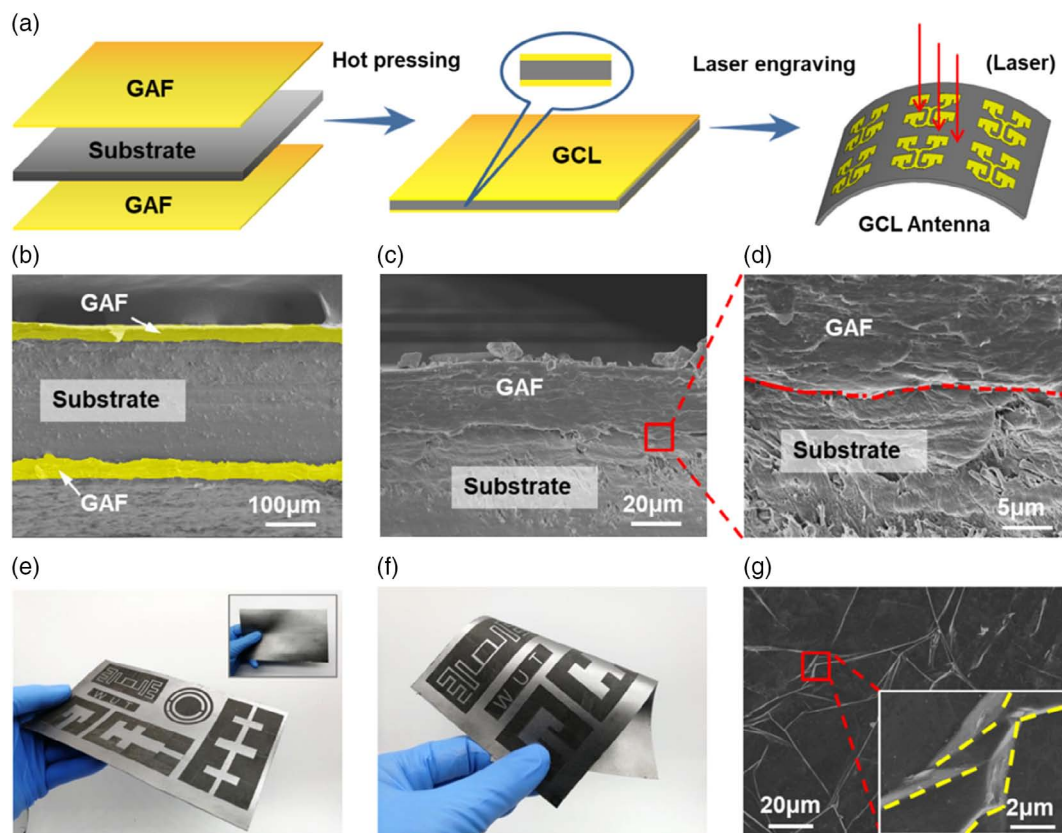


**Figure 2.** a) The schematic diagram of GCL and antenna based on the GCL preparation process. b) Cross-sectional SEM image of GCL shows the sandwich structure. c,d) Zoomed-in images of (b) (red dashed lines stand for the interface between GAF and substrate). e,f) Digital photographs of GCL carved into various devices with high flexibility. g) SEM image of the surface of GCL with the inset showing the zoomed-in image of the micro-folds (yellow dashed lines stand for the micro-folds).



exhibited in Figure 2g, which illustrates the reasons for the good flexibility of GCL: after static calendaring, the micro-gasbags of GAF are compressed, resulting in many micro-folds on the surface and inside. When it is bent under force, the micro-folds are straightened to avoid the breakage of GCL and to prevent detachment from the substrate. After flattening, the straightened micro-folds are restored to their original shape, rendering the GCL with high flexibility and stability.<sup>[33]</sup>

The element energy dispersion spectrum (EDS) of the interface of GCL is explored to further prove the composite situation of the conductive layer and the dielectric layer. **Figure 3a** shows the cross-sectional SEM image of GCL with the white line indicating the track of EDS scanning from top to bottom. There are no apparent structural defects, such as cavities and cracks at the interface of GAF/substrate, which indicates the successful formation of a close connected interface between GAF and substrate. **Figure 3b** shows the element distribution along the white line in **Figure 3a**. The intensity of fluorine significantly

decreases to near zero at the interface, because the substrate is mainly composed of carbon and fluorine, whereas GAF is composed of carbon only. Notably, the intensity of oxygen peak barely fluctuates at the interface, indicating no defects have been introduced on the both GAF and substrate surface due to the vacuum hot pressing process. To test structural stability and bonding of GAF and substrate, GAF is stripped from GCL by mechanically peeled off with tapes. As shown in **Figure 3c**, after mechanical stripping of GAF, there still existed continuous residual GAF with a thickness of 6  $\mu\text{m}$  on the substrate (the original thickness of GAF before stripping on substrate is around 25  $\mu\text{m}$ ), and the bonding interface of GAF/substrate exhibited no structural defects. It is proved that after stripping, the interlayer of GAF teared, and the interface of GAF/substrate remained integrated, which suggests that the interfacial adhesion between GAF and substrate is stronger than interlayer adhesion of GAF. **Figure 3d** shows the element distribution along the white line in **Figure 3c**. The intensity of oxygen

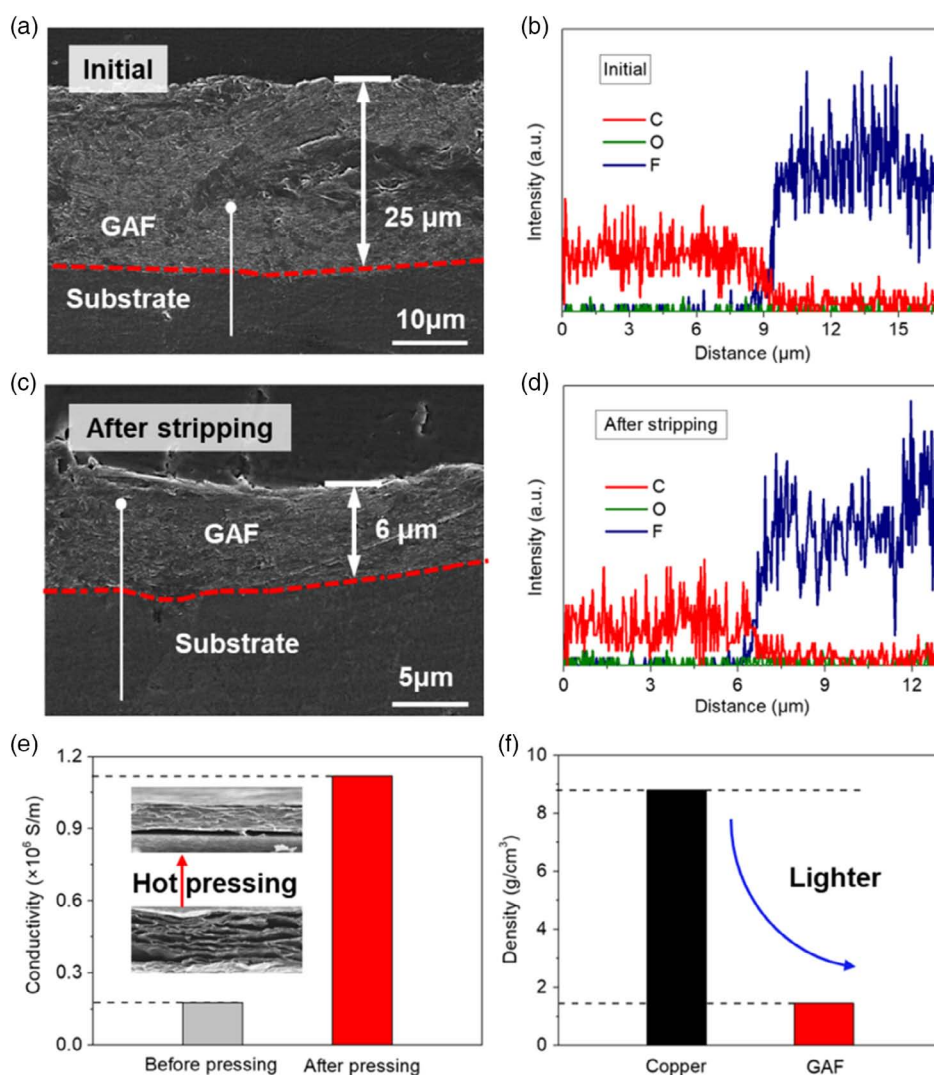


**Figure 3.** a) Cross-sectional SEM image of initial GCL (the white line is the track of EDS line scanning, from top to bottom). b) Element distribution along the white line in (a). c) Cross-sectional SEM image of GCL after stripping of GAF. d) Element distribution along the white line in (c). e) Comparison of GAF conductivity before and after hot pressing. f) Density comparison of copper and GAF.

exhibited no fluctuation at the GAF/substrate interface after stripping of GAF, which further demonstrates the good interfacial stability of the GAF/substrate interface. It is worth to mention that the conductivity of the GAF is increased after hot pressing. As shown in Figure 3e, the conductivities of GAF before and after vacuum hot pressing are  $1.76 \times 10^5$  and  $1.12 \times 10^6 \text{ S m}^{-1}$ , respectively. The hot pressing makes the GAF more compact, which increases the contact area between graphene sheets, which reduces the contact resistance, and, thus, improves the conductivity of GAF. In addition, the density of copper, the traditional PCB conductor material, and GAF are compared, as shown in Figure 3f. The density of GAF is measured to be  $1.45 \text{ g cm}^{-3}$ , which is only one-sixth of that of copper ( $8.8 \text{ g cm}^{-3}$ ). The GCL parameters compared with CCL are listed in Table S1, Supporting Information.

To further explore the properties of GCL as a PCB, a 5G millimeter wave antenna array based on GCL is designed. The designed antenna operates at 26 GHz. Figure 4a shows the schematic of antenna element with a dimension of  $10 \text{ mm} \times 9 \text{ mm}$ . The width ( $W$ ) and the length ( $L$ ) of element patch can be calculated from the following equations<sup>[34]</sup>

$$W = \frac{1}{2f_0\sqrt{\mu_0\epsilon_0}}\sqrt{\frac{2}{\epsilon_r + 1}} \quad (1)$$

$$L = \frac{1}{2f_0\sqrt{\epsilon_e\mu_0\epsilon_0}} - 2\Delta L \quad (2)$$

$$\Delta L = 0.412h \frac{(\epsilon_e + 0.3)(W/h + 0.264)}{(\epsilon_e - 0.258)(W/h + 0.8)} \quad (3)$$

$$\epsilon_e = (\epsilon_r + 1)/2 + (\epsilon_r - 1)/2[1 + 12h/W]^{-1/2} \quad (4)$$

where  $f_0$  is the resonant frequency of antenna,  $\mu_0$  and  $\epsilon_0$  are the vacuum permeability and permittivity, respectively, and  $\epsilon_e$  is the effective dielectric constant. The optimized dimension of patch is  $4.63 \text{ mm} \times 3.61 \text{ mm}$ . Recessed microstrip-line feed is an effective way to reduce the size of antenna. The input resistance of antenna and impedance of microstrip line ( $50 \Omega$ ) can be matched by changing the inset depth ( $y_0$ ). When  $y_0 = 1.26 \text{ mm}$ , the input resistance of antenna patch is  $50 \Omega$ . The width ( $W_0$ ) and the length ( $L_0$ ) of the microstrip-line feed are  $W_0 = 1.57 \text{ mm}$  and  $L_0 = 3.76 \text{ mm}$ , respectively.

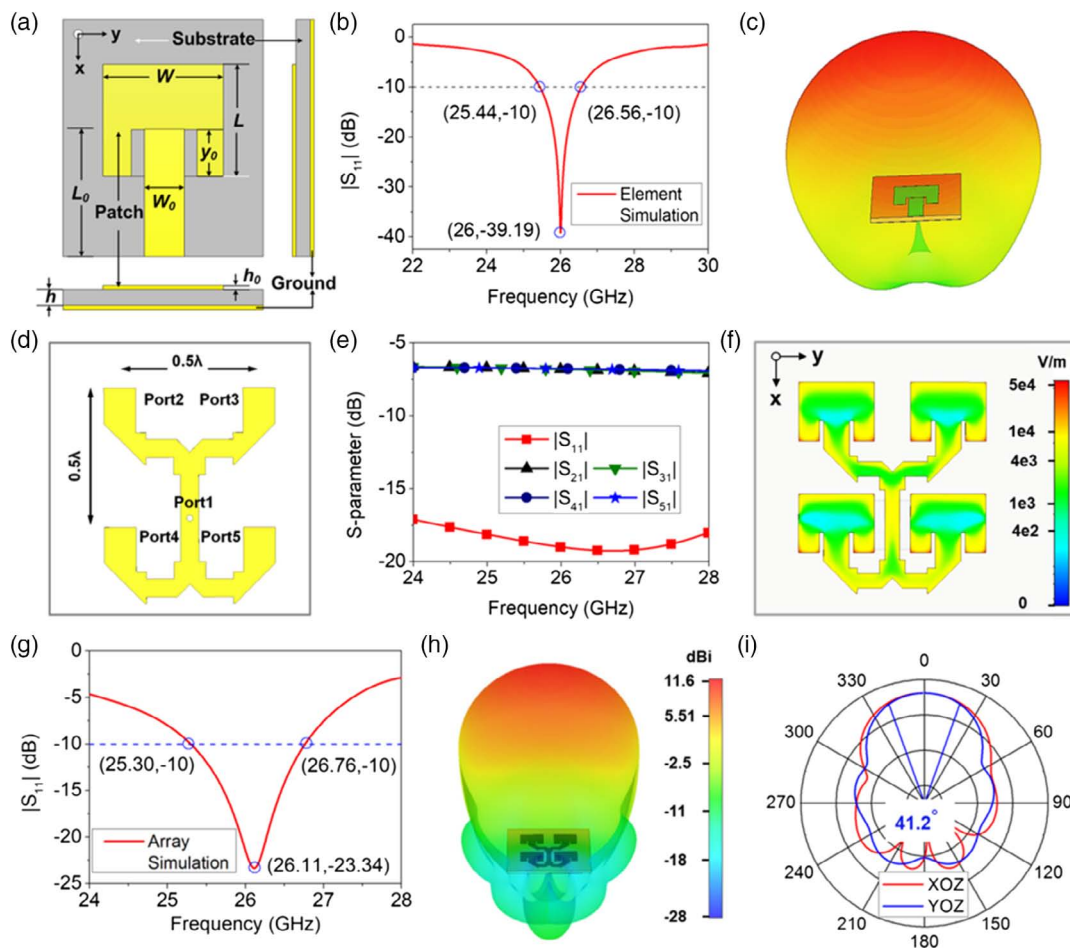


**Figure 4.** a) The schematic illustration of GAF antenna element with a dimension of  $10 \text{ mm} \times 9 \text{ mm}$  (the yellow parts are the conductive layers, and the gray part is the substrate). b,c) Simulated  $|S_{11}|$  response and 3D radiation pattern of antenna element, respectively. d) The structure of feed network (T-type power divider). e) Simulated S-parameters of feed network. f) E-field distribution of GCL antenna array. g) Simulated  $|S_{11}|$  response of antenna array. h) The 3D radiation pattern of GCL antenna array. i) Radiation patterns of GCL antenna array in XOZ-plane (red) and YOZ-plane (blue).

The reflection coefficient ( $|S_{11}|$ ) of GCL antenna element is simulated, as shown in Figure 4b. As it can be seen, the GCL antenna element resonates at 26 GHz with the minimum reflection of  $-39.19$  dB. The  $-10$  dB impedance bandwidth is from 25.44 to 26.56 GHz. The radiation patterns of antenna element are shown in Figure 4c and Figure S4, Supporting Information. It is noteworthy that the highest gain at 26 GHz is 7.41 dBi, and the half power widths are  $78.2^\circ$  and  $78.4^\circ$  of XOZ-plane and YOZ-plane, respectively. All results indicate the good performances of the antenna and its suitability as array element. Moreover, appropriate feed network is crucial for antenna array. In this work, a T-type power divider with equal amplitude and phase is used to design the antenna array feed network, as shown in Figure 4d. Port 1 is the input port, and ports 2–5 are the output ports. To reduce mutual coupling between two adjacent antenna elements and suppress the grating lobes, the spacing between adjacent elements is determined to be  $0.5\lambda$  ( $\lambda$  is the operating wavelength at 26 GHz in free space). Figure 4e shows the simulated S-parameters of the feed network. The reflection coefficient of input port 1 is  $-18.98$  dB, and all output ports 2–5 have the similar transmission coefficients of  $-6.7$  dB at 26 GHz. The results indicate that the feeder networks transmit energy with high efficiency and distribute the energy equally to four output ports with low insertion loss.

The design of the GCL antenna array structure with a dimension of  $1.3\lambda \times 1.3\lambda$  is completed by simulations of the elements and feeder network, as shown in Figure S5, Supporting Information. The surface E-field distribution of GCL antenna array gives in-depth information of the radiation characteristics of the antenna, as shown in Figure 4f. It can be seen from the results that, at 26 GHz, the E-field mainly distributes at the edge

of the patch, which conforms to the slot radiation mode of microstrip antenna. In addition, it is observed that the electric field is evenly distributed on the feeder network and has the same amplitude in four output feeder ports, which proves that the designed feeder network impedance matches well and achieves uniform distribution of power. Figure 4g is the simulated reflection coefficient of GCL antenna array resonated at 26.11 GHz. The antenna array exhibits a good  $|S_{11}|$  of  $-23.34$  dB and the  $-10$  dB impedance bandwidth of 25.30–26.76 GHz, which is better than the antenna element shown in Figure 4b. To better explore the radiation characteristics of GCL antenna array, the gain and radiation patterns are simulated, as shown in Figure 4h,i and Figure S6, Supporting Information. It is obvious that the radiation pattern beam of the antenna array is much narrower than that of the element antenna. The maximum gain is 11.6 dBi at 26 GHz, and the half power widths are  $41.2^\circ$  and  $41.4^\circ$  in the XOZ-plane and YOZ-plane, respectively. High gain and narrow beam enable antenna to detect and communicate more accurately.

To experimentally validate the properties of the proposed GCL antenna array, we fabricate the antenna array with high forming precision, as shown in Figure 5a and Figure S7, Supporting Information. Before measuring, the antenna measurement system is calibrated with the calibrator of Keysight 85058B to compensate for the loss of coaxial lines and connections. To demonstrate the performances of the GCL antenna array, a copper antenna array based on the CCL that operates at the same frequency is also fabricated and measured. Figure 5b plots the reflection coefficient responses of GCL (red line) and CCL (black line) antenna array measured by vector network analyzer (VNA; Keysight N5247A). The resonant frequency of GCL

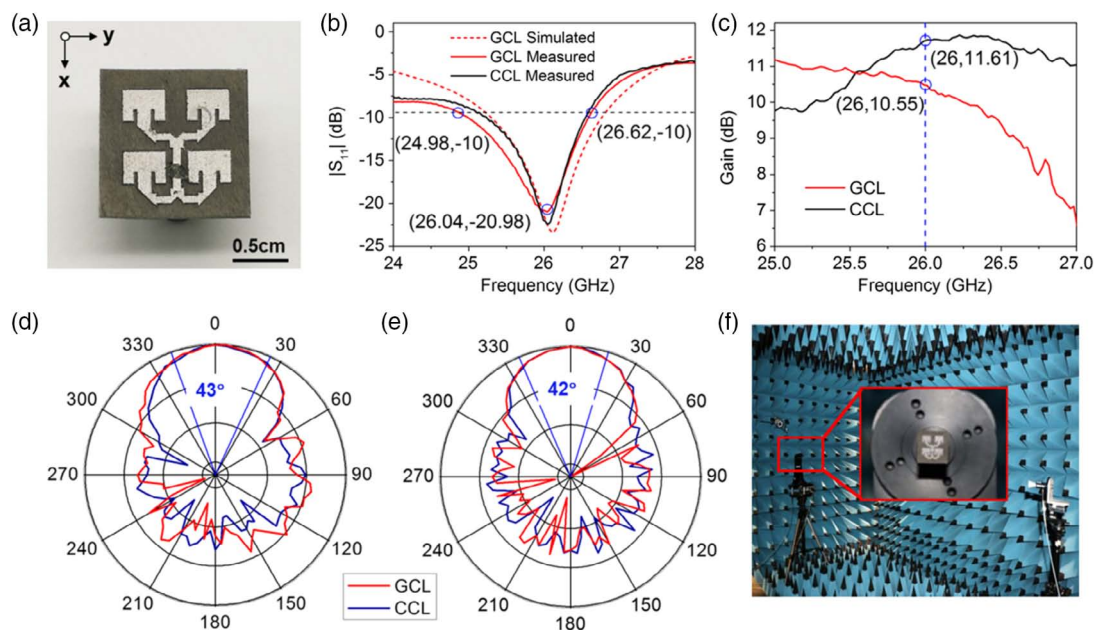


**Figure 5.** a) The digital photograph of GCL antenna array with a dimension of  $1.3\lambda \times 1.3\lambda$ . b) Measured  $|S_{11}|$  response of GCL (red line) and CCL (black line) antenna arrays. The simulated  $|S_{11}|$  response of GCL antenna array (red dashed line) is also included for comparison. c) Measured gain response of GCL (red line) and CCL (black line) antenna arrays. d,e) A comparison of measured radiation patterns of GCL (red) and CCL (blue) antenna arrays in d) XOZ-plane and e) YOZ-plane. f) Measurement environment of radiation patterns with the inset showing the zoomed-in image of the positioner platform.

antenna array is 26.04 GHz with the  $|S_{11}|$  of  $-20.98$  dB, which is similar to that of the CCL antenna array. The measured impedance bandwidth of the GCL antenna array of 24.98–26.62 GHz is, however, better than the CCL antenna array of 25.06–26.14 GHz. As shown in Figure 5c, the realized gain of GCL antenna array is 11.05 dBi at 26 GHz, which is similar to the simulation result of 11.6 dBi. The higher loss in measurement results is due to the contact resistance and a mismatch of  $50\ \Omega$  impedance between antenna and connector in experiments. Figure 5e also shows that the gain of GCL is comparable to that of the CCL antenna array (11.61 dBi), indicating that the radiation efficiency of GCL antenna array is 95.18% if the CCL antenna array is 100%. It is worth noting that the gain of the GCL antenna array maintains above 10 dBi between 25 and 26.48 GHz and is higher than the CCL antenna array below 25.73 GHz. The frequency offset of maximum gain is caused by the asymmetrical radiation patterns, which can indicate directionality, radiation power distribution, and magnitude of antenna. Moreover, to experimentally measure the radiation patterns, fixed standard gain horn antenna is used as the radiating antenna, and the GCL antenna array is fixed on the turntable as the receiving antenna. The data are recorded for every  $1^\circ$  rotation. Figure 5d,e shows the measured radiation patterns in the XOZ-plane and YOZ-plane of the GCL antenna array at 26 GHz with a half power width of  $43^\circ$  and  $42^\circ$ , respectively. Significantly, the radiation patterns are very similar to the CCL antenna array. In addition, all the measurement processes are carried out in the microwave anechoic chamber, as shown in Figure 5f.

### 3. Conclusion

In conclusion, for the first time, the binder-free GCLs with excellent electronic conductivity and lightweight for flexible PCB application are prepared by a vacuum-assistant hot pressing method. We applied this GCL structure in a 5G millimeter wave antenna array fabrication. As a result, the GCL-based antenna array shows nearly similar return loss, radiation patterns, and realized gain to the commercial copper PCB-based antenna array. Moreover, the GCL antenna has a better bandwidth of 1.64 GHz than a CCL of 1.08 GHz. Therefore, the high-conductivity, lightweight, and flexible GCL as a new generation of PCB have great application values in the field of flexible electronic and wearable devices.

### 4. Experimental Section

**Preparation of GAF:** The commercially available GO was purchased from Wuxi chengyi education technology Co. Ltd. It was diluted with ultrapure water to get the GO suspension with a mass fraction of 2.5%. The GO suspension was then coated onto polyethylene terephthalate (PET) substrate and dried at room temperature for 12 h to obtain the GO assembled films. Thereafter, the GO assembled films were annealed at  $1300^\circ\text{C}$  for 2 h and then  $2850^\circ\text{C}$  for 1 h in continuously flowing argon (Ar) atmosphere to obtain the GAFs.

**Preparation of GCL:** First, the GAFs were placed on both sides of the pre-prepared flexible composite substrate (Rogers 5880) with no additional binder and clamped in two specular steel plate templates as the sample to be pressed. The sample was then pressed with a pressure of 8 MPa and heated to  $380^\circ\text{C}$  at a rise rate of  $8^\circ\text{C}\ \text{min}^{-1}$  in vacuum.

At the sintering temperature of  $380^\circ\text{C}$ , the pressure was increased to 12 MPa and held for 100 min. Finally, the GCL was obtained after cooling to room temperature.

**Antenna Design and Fabrication:** The carving path of the antenna dimensions was calculated using LPKF CircuitPro PL 2.0 to match the laser engraving machine. Laser engraving machine (LPKF Laser & Electronics ProtoLaser S) fabricated the antenna in one-step refer to the calculated laser path with a resolution of  $25\ \mu\text{m}$ .

**Characterization:** Field-emission transmission electron microscope (FETEM) results were measured by Talos F200S. Field-emission scanning electron microscopy (FESEM) images were obtained with JEOL JSM-7610F. The superlarge depth image is taken by a 3D microscopic system (KEYENCE, VHX-600E). XRD experiments were carried out by a Rigaku Smartlab SE instrument using Ni-filtered  $\text{Cu}\ K\alpha$  radiation. Raman spectra were recorded by the LabRAM HR Evolution Raman Spectrometer. The element EDS was recorded by Hitachi S-4800.

### Supporting Information

Supporting Information is available from the Wiley Online Library or from the author.

### Acknowledgements

This work was financially supported by 2018 National Key R&D Program of China 257, the National Natural Science Foundation of China (No. 51701146, 51572205 and 51672204), the Equipment Pre-Research Joint Fund of EDD and MOE (No. 614A02022262), Foundation of National Key Laboratory on Electromagnetic Environment Effects (No.614220504030617), and the Fundamental Research Funds for the Central Universities (No. 2020-YB-032, 205209016).

### Conflict of Interest

The authors declare no conflict of interest.

### Keywords

5G millimeter wave antenna, binder-free, flexible printed circuit board, graphene assembled film, graphene clad laminate

Received: April 14, 2020

Revised: May 4, 2020

Published online:

- [1] M. Gomes, S. Cruz, H. Lopes, B. Arcipreste, R. Magalhaes, A. F. Da Silva, J. C. Viana, *IEEE Trans. Ind. Electron.* **2019**, *66*, 8181.
- [2] D. Moschou, L. Greathead, P. Pantelidis, P. Kelleher, H. Morgan, T. Prodromakis, *Biosens. Bioelectron.* **2016**, *86*, 805.
- [3] I. Puchades, J. E. Rossi, C. D. Cress, E. Naglich, B. J. Landi, *ACS Appl. Mater. Inter.* **2016**, *8*, 20986.
- [4] C. Ning, C. S. K. Lin, D. C. W. Hui, G. McKay, *Top. Curr. Chem.* **2017**, *375*, 43.
- [5] F. P. C. Silvas, M. M. Jiménez Correa, M. P. K. Caldas, V. T. de Moraes, D. C. R. Espinosa, J. A. S. Tenório, *Waste Manage.* **2015**, *46*, 503.
- [6] P. Hadi, M. Xu, C. Lin, C. Hui, G. McKay, *J. Hazard. Mater.* **2015**, *283*, 234.
- [7] W. Zhou, C. Liu, R. Song, X. Zeng, B. Li, W. Xia, J. Zhang, G. Huang, Z. P. Wu, D. He, *Appl. Phys. Lett.* **2019**, *114*, 113503.
- [8] S. N. H. Sa Don, M. R. Kamarudin, F. Ahmad, M. Jusoh, H. A. Majid, *Appl. Phys. A* **2017**, *123*, 118.



- [9] R. Song, Q. Wang, B. Mao, Z. Wang, D. Tang, B. Zhang, J. Zhang, C. Liu, D. He, Z. Wu, S. Mu, *Carbon* **2018**, *130*, 164.
- [10] E. Amram Bengio, D. Senic, L. W. Taylor, R. J. Headrick, M. King, P. Chen, C. A. Little, J. Ladbury, C. J. Long, C. L. Holloway, A. Babakhani, J. C. Booth, N. D. Orloff, M. Pasquali, *Appl. Phys. Lett.* **2019**, *114*, 203102.
- [11] L. Tao, K. Zhang, H. Tian, Y. Liu, D. Wang, Y. Chen, Y. Yang, T. Ren, *ACS Nano* **2017**, *11*, 8790.
- [12] S. P. Milovanović, M. Ž. Tadić, F. M. Peeters, *Appl. Phys. Lett.* **2017**, *111*, 43101.
- [13] Y. Fujisaki, H. Koga, Y. Nakajima, M. Nakata, H. Tsuji, T. Yamamoto, T. Kurita, M. Nogi, N. Shimidzu, *Adv. Funct. Mater.* **2014**, *24*, 1657.
- [14] Q. Cao, H. Kim, N. Pimparkar, J. P. Kulkarni, C. Wang, M. Shim, K. Roy, M. A. Alam, J. A. Rogers, *Nature* **2008**, *454*, 495.
- [15] D. Sun, M. Y. Timmermans, Y. Tian, A. G. Nasibulin, E. I. Kauppinen, S. Kishimoto, T. Mizutani, Y. Ohno, *Nat. Nanotechnol.* **2011**, *6*, 156.
- [16] D. Sun, M. Y. Timmermans, A. Kaskela, A. G. Nasibulin, S. Kishimoto, T. Mizutani, E. I. Kauppinen, Y. Ohno, *Nat. Commun.* **2013**, *4*, 2302.
- [17] E. Amram Bengio, D. Senic, L. W. Taylor, D. E. Tsentalovich, P. Chen, C. L. Holloway, A. Babakhani, C. J. Long, D. R. Novotny, J. C. Booth, N. D. Orloff, M. Pasquali, *Appl. Phys. Lett.* **2017**, *111*, 163109.
- [18] J. Hirotsu, Y. Ohno, *Top. Curr. Chem.* **2019**, *377*, 3.
- [19] M. S. Fuhrer, J. Nygård, L. Shih, M. Forero, Y. Yoon, M. S. C. Mazzoni, H. J. Choi, J. Ihm, S. G. Louie, A. Zettl, P. L. McEuen, *Science* **2000**, *288*, 494.
- [20] A. Znidarsic, A. Kaskela, P. Laiho, M. Gaberscek, Y. Ohno, A. G. Nasibulin, E. I. Kauppinen, A. Hassanien, *J. Phys. Chem. C* **2013**, *117*, 13324.
- [21] Y. Bayram, Y. Zhou, B. S. Shim, S. Xu, J. Zhu, N. A. Kotov, J. L. Volakis, *IEEE Trans. Antenn. Propag.* **2010**, *58*, 2732.
- [22] N. A. Vacirca, J. K. McDonough, K. Jost, Y. Gogotsi, T. P. Kurzweg, *Appl. Phys. Lett.* **2013**, *103*, 73301.
- [23] G. Xin, T. Yao, H. Sun, S. M. Scott, D. Shao, G. Wang, J. Lian, *Science* **2015**, *349*, 1083.
- [24] N. Zhang, Z. Wang, R. Song, Q. Wang, H. Chen, B. Zhang, H. Lv, Z. Wu, D. He, *Sci. Bull.* **2019**, *64*, 540.
- [25] Z. Wang, B. Mao, Q. Wang, J. Yu, J. Dai, R. Song, Z. Pu, D. He, Z. Wu, S. Mu, *Small* **2018**, *14*, 1704332.
- [26] S. Feng, T. Yao, Y. Lu, Z. Hao, S. Lin, *Nano Energy* **2019**, *58*, 63.
- [27] Y. Liu, P. Li, F. Wang, W. Fang, Z. Xu, W. Gao, C. Gao, *Carbon* **2019**, *155*, 462.
- [28] Y. Wen, M. Wu, M. Zhang, C. Li, G. Shi, *Adv. Mater.* **2017**, *29*, 1702831.
- [29] L. Wang, Q. Wen, P. Jia, M. Jia, D. Lu, X. Sun, L. Jiang, W. Guo, *Adv. Mater.* **2019**, *31*, 1903029.
- [30] D. Tang, Q. Wang, Z. Wang, Q. Liu, B. Zhang, D. He, Z. Wu, S. Mu, *Sci. Bull.* **2018**, *63*, 574.
- [31] K. Pan, Y. Fan, T. Leng, J. Li, Z. Xin, J. Zhang, L. Hao, J. Gallop, K. S. Novoselov, Z. Hu, *Nat. Commun.* **2018**, *9*, 5110.
- [32] B. Liu, F. Yin, X. Dai, J. He, W. Fang, C. Chen, Y. Dong, *Mater. Sci. Eng. A* **2017**, *679*, 172.
- [33] L. Peng, Z. Xu, Z. Liu, Y. Guo, P. Li, C. Gao, *Adv. Mater.* **2017**, *29*, 1700589.
- [34] R. Song, G. Huang, C. Liu, N. Zhang, J. Zhang, C. Liu, Z. P. Wu, D. He, *Int. J. RF Microw. Comput.-Aided Eng.* **2019**, *29*, e21692.